Draft version February 5, 2008
Preprint typeset using LaTeX style emulateapj v. 02/09/03

arXiv:astro-ph/0610949v1 31 Oct 2006

MAGNETIZED NON-LINEAR THIN SHELL INSTABILITY: NUMERICAL STUDIES IN 2D

Fabian Heitsch[1], Adrianne D. Slyz[2,3], Julien E.G. Devriendt[2], Lee W. Hartmann[1], and Andreas Burkert[4]

Draft version February 5, 2008

ABSTRACT

We revisit the analysis of the Non-linear Thin Shell Instability (NTSI) numerically, including magnetic fields. The magnetic tension force is expected to work against the main driver of the NTSI – namely transverse momentum transport. However, depending on the field strength and orientation, the instability may grow. For fields aligned with the inflow, we find that the NTSI is suppressed only when the Alfvén speed surpasses the (supersonic) velocities generated along the collision interface. Even for fields perpendicular to the inflow, which are the most effective at preventing the NTSI from developing, internal structures form within the expanding slab interface, probably leading to fragmentation in the presence of self-gravity or thermal instabilities. High Reynolds numbers result in local turbulence within the perturbed slab, which in turn triggers reconnection and dissipation of the excess magnetic flux. We find that when the magnetic field is initially aligned with the flow, there exists a (weak) correlation between field strength and gas density. However, for transverse fields, this correlation essentially vanishes. In light of these results, our general conclusion is that instabilities are unlikely to be erased unless the magnetic energy in clouds is much larger than the turbulent energy. Finally, while our study is motivated by the scenario of molecular cloud formation in colliding flows, our results span a larger range of applicability, from supernovae shells to colliding stellar winds.

Subject headings: instabilities — MHD — turbulence — methods:numerical — ISM:clouds — ISM: magnetic fields

1. MOTIVATION

Shocks and shells exist abundantly in the interstellar medium (ISM). Driven by supernovae, expanding HII-regions, gravitational flows or wholesale cloud collisions, they not only strongly influence the ISM dynamics, but also affect its chemistry. However, structural analyses of the ISM show spectral indices closer to the Kolmogorov value of incompressible turbulence (see Elmegreen & Scalo 2004 for a review). Independently of the problem of how well these indices constrain the type of turbulence, there are plenty of physical mechanisms to explain the closeness to the Kolmogorov value, ranging from the intrinsic nature of MHD turbulence (e.g. Goldreich & Sridhar 1995, Boldyrev et al. 2002, Cho & Lazarian 2003) to the conversion of compressible to solenoidal modes (Falgarone et al. 1994, Elmegreen & Scalo 2004).

It is the latter mechanism that motivated this study. In the absence of shear flows (oblique shocks) and thermal instabilities, the Non-linear Thin Shell Instability (Vishniac 1994) provides a natural mechanism to convert compressible motions into solenoidal ones. The NTSI is a rippling instability, relying on transverse momentum transport due to bends in the collision interface of two opposing flows. It is likely to arise in a wide range of environments, from colliding stellar winds, supernova shells, colliding HI streams/clouds, to galaxy mergers.

[1] Dept. of Astronomy, University of Michigan, 500 Church St., Ann Arbor, MI 48109-1042, U.S.A
[2] Université Claude Bernard Lyon 1, CRAL, Observatoire de Lyon, 9 Avenue Charles André, 69561 St-Genis Laval Cedex, France; CNRS, UMR 5574; ENS Lyon
[3] Oxford University, Astrophysics, Denys Wilkinson Building, Keble Road, Oxford, OX1 3RH, United Kingdom
[4] University Observatory Munich, Scheinerstr. 1, 81679 Munich, Germany

The NTSI has been widely studied numerically (see Heitsch et al. 2006 for a summary of the literature), mostly focusing on the effects of self-gravity and thermal instabilities. Our interest in the NTSI comes from the role it plays in the evolution of molecular clouds in colliding HI flows (Heitsch et al. 2005, 2006; Vázquez-Semadeni et al. 2006), but the results have a wider applicability. With the exception of Klein & Woods (1998), who included the magnetic pressure term in their study of cloud collisions, work on the NTSI has so far neglected the effect of magnetic fields. However, fields could have a deciding influence on the evolution of a shock-bounded slab. Motivated by the numerical models of Vázquez-Semadeni et al. (1995) and Passot et al. (1995), Hartmann et al. (2001) and Bergin et al. (2004) suggested that fields could, in fact, lead to a selection effect for molecular cloud formation: clouds can only form if the fields are aligned with the flows assembling the gas.

As a first step, we revisit the isothermal analysis of Vishniac (1994) numerically, and study the evolution of the NTSI in a two-dimensional, magnetohydrodynamical environment. While the general expectation (§2 2.1) is met in the laminar case, namely that magnetic fields can efficiently damp the NTSI, the geometry of the rippled interface induces non-ideal MHD effects, requiring a numerical method capable of handling such effects in a stable and accurate way (§2 2.2). However, we find that the exact amount of dampening crucially depends on the field orientation and strength (§3). This is especially true in the turbulent case, where turbulent reconnection inside the over-pressured slab leads to a pressure deficit, thus compressing the gas even further. Finally, we show that the correlation between field strength and gas density is at best weak, even in the case of fields perpendicularly oriented with respect to the inflow, for which the

field would be expected to scale linearly with the density.

2. PHYSICS AND NUMERICS

2.1. *Physics*

The growth rate of the NTSI is mostly controlled by $k\eta$, the product of the wave number of the slab perturbation k, and the amplitude of the slab's initial displacement η (equivalently, the amplitude of the collision interface's geometrical perturbation). The instability is driven by lateral transport of longitudinal momentum, i.e. if the inflow is parallel to the x direction, and the slab is in the y-z-plane, x-momentum is transported laterally in y (and z), collecting at the focal points of the perturbed slab. The efficiency of lateral momentum transport is key to the development of the instability, since it is the imbalance of ram pressure at the focal points that eventually propels matter forward, driving the growth of the slab's perturbation. Vishniac (1994) derived a growth rate of

$$\omega \approx c_s k (k\eta)^{1/2}, \tag{1}$$

with the sound speed c_s. Blondin & Marks (1996) found that at constant η and for small ks, equation (1) yields only a lower limit, while for large ks, the analytical growth rates agree well with the numerical results. The reason for this seems to lie in the efficiency of deflecting the incoming flow: for small ks, a small fraction of the incoming flow's momentum is converted to lateral motions, while a large part compresses the slab (depending on the equation of state, this could lead to an increase in energy losses).

After the initial growth-phase (eq. [1]), the NTSI reaches saturation through two mechanisms: (i) expansion of the slab which stops the lateral momentum transport by preventing the inflow from reaching the focal points, and (ii) shear flow (Kelvin-Helmholtz) instabilities (KHI) in regions of the slab connecting the focal points. The KHIs both generate inner structure and revive the slab's expansion. Note that strong cooling (not modeled here) can also suppress the NTSI via early fragmentation (Hueckstaedt 2003).

Qualitatively, we expect magnetic fields to prevent the NTSI and subsequent KHI-modes from occurring. However, the detailed quantitative extent of the damping should depend on the orientation of the field with respect to the inflow. Indeed, fields aligned with the inflow resist instabilities via the magnetic tension force, and therefore should be more efficient in suppressing the NTSI when $k\eta$ is small, even though the strong pairwise field reversals arising from the opposed shear velocities along the slab (see §3 3.1) could trigger reconnection. On the other hand, fields perpendicular to the inflow (but still in the 2D plane), primarily prevent instabilities from growing because of the magnetic pressure term in the Lorentz force, and to a lesser extent, because of magnetic tension. For the sake of completeness, we mention that the third possible field configuration in 2D, i.e. the one in which the magnetic field is perpendicular to the flow plane, is irrelevant for this study since in that case the gas behaves as a system with an adiabatic exponent of 2 for which the NTSI cannot be excited (Vishniac 1994).

2.2. *Numerics*

The magnetohydrodynamical scheme[5] is based on a conservative gas-kinetic flux-splitting method, introduced by Xu (1999) and Tang & Xu (2000) and derived from the 1st-order BGK (Bhatnagar et al. 1954) model. Representing the velocity distributions as Maxwellians in each cell, fluxes across cell walls are derived from the differences in the velocity moments of Maxwellian distributions reconstructed at the cell walls. The reconstruction is second order in space using MUSCL limiters, and it allows a fast and consistent way to implement viscosity and Ohmic resistivity in the form of dissipative fluxes (Heitsch et al. 2004) at close to zero extra computing cost, while preserving the time order of PROTEUS since the dissipative terms are not simply added as source terms but are part of the flux computation. This allows us to control dissipation in a physical manner, without having to rely on numerical dissipation to terminate the turbulent cascade at grid scale. Total energy is conserved at machine-accuracy level for an adiabatic equation of state. In the isothermal version which we are using in §3, the total energy equation is not evolved. PROTEUS uses a 2nd order TVD Runge-Kutta time stepping (Shu & Osher 1988) for the MHD equations to achieve 2nd order temporal accuracy. Fluxes are updated in time-unsplit fashion, i.e. flux updates for spatial directions are computed using the initial conditions of the current time step. In order to keep $\nabla \cdot \mathbf{B} = 0$, PROTEUS employs a Hodge projection (Balsara 1998; Zachary et al. 1994). The code is fully message passing interface (MPI) parallelized.

With PROTEUS, one may switch between the MHD-solver previously described and a purely hydrodynamical solver based on the 2nd-order BGK model. The latter implementation has been introduced and extensively discussed by Prendergast & Xu (1993), Slyz & Prendergast (1999), Heitsch et al. (2006) and Slyz et al. (2006), and we therefore refer the reader interested in implementation details to these papers.

One-dimensional shock tests and the Orszag-Tang vortex have already been discussed by Tang & Xu (2000), hence in what follows, we focus on three other MHD test cases. The two first ones, i.e. the propagation of a linear Alfvén wave under resistive damping (§2 2.2 2.2.1) and the current sheet evolution (§2 2.2 2.2.2) are both meant to test the resistive fluxes, while the third one, i.e. the advection of a field loop (§2 2.2 2.2.3) is a geometry test. A detailed study of the magnetized Kelvin-Helmholtz Instability is under way (Palotti et al. 2006).

2.2.1. *Propagation of a linear Alfvén Wave*

This one-dimensional test checks the resistive flux implementation as well as the accuracy of the overall scheme. A linear Alfvén wave under weak Ohmic dissipation is damped at a rate of

$$\omega_i = \frac{1}{2}\lambda_\Omega k^2, \tag{2}$$

[5] We called the scheme PROTEUS, under which name we will refer to it subsequently. Proteus is a lesser god in Greek mythology, also known as "The Old Man of the Sea". He lives in the sea off the coast of Egypt and can see things in the past, presence and future, but is very unwilling to share his knowledge. In order to evade questions, he has the ability to change his appearance. However, if you manage to catch and hold him, he will assume his true shape and answer your questions.

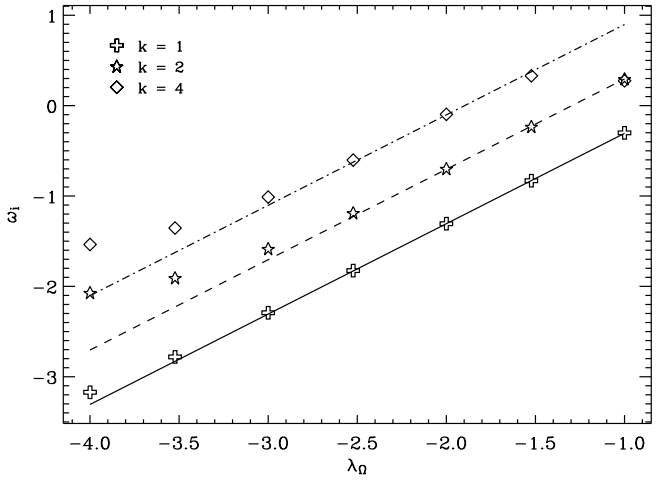

FIG. 1.— Damping rate (eq. [2]) of a linear Alfvén wave against Ohmic resistivity for $\kappa = 1, 2, 4$. The resolution is $N = 64$. Errors of the measured damping rates are smaller than the symbol sizes. Lines denote the analytical solution.

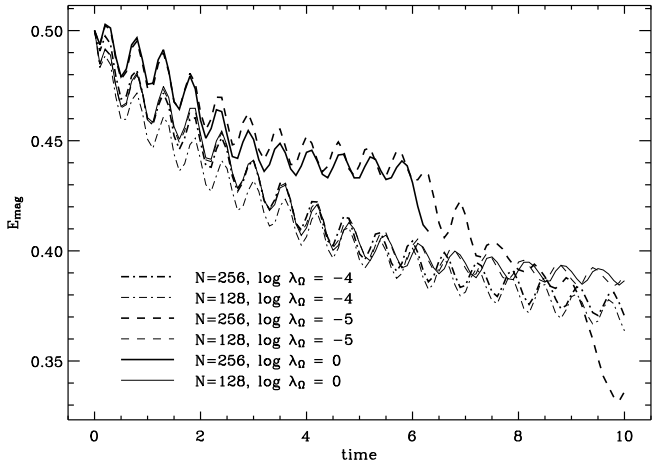

FIG. 2.— Total magnetic energy against time for the current sheet test. A finite resistivity λ_Ω helps stabilize the code.

where λ_Ω is the Ohmic resistivity, and $k = 2\pi\kappa/L$ is the wave number of the Alfvén wave, with $\kappa \in \mathbb{N}$. The strongly damped case, where the decay dominates the time evolution, is physically uninteresting for our application, since the Ohmic resistivity is mainly used to control numerical dissipation. Figure 1 shows the damping rate against Ohmic resistivity λ_Ω for $\kappa = 1, 2, 4$ at a grid resolution of $N = 64$.

From Figure 1, it is clear that, as one diminishes the value of λ_Ω, there comes a point when the numerical resistivity of the scheme becomes comparable to the physical one, causing the measured damping rate to flatten out and depart from the analytical solution. For $\kappa = 4$ and $\lambda_\Omega = 0.1$, the wave decays too quickly to allow a reliable measurement, and the system enters the strongly damped branch of the dispersion relation. However, we emphasize that, even for this high value of κ in light of the modest resolution we used, the resistivity range available to PROTEUS spans three orders of magnitude.

2.2.2. *Current Sheet*

This test is taken from Hawley & Stone (1995) and the ATHENA test suite[6]. A square domain of extent $-0.5 \le x, y \le 0.5$ and of constant density $n_0 = 1$ and pressure p_0 is permeated by a magnetic field along the y direction such that $B_y(|x| < 0.25) = \sqrt{4\pi}$, and $B_y = -\sqrt{4\pi}$ elsewhere. This results in two magnetic null lines, which then are perturbed by velocities $v_x = A\sin(2\pi y)$. The goal is to find the pressure p_0 and velocity amplitude A for which the code crashes. The main problem is – especially in conservative schemes – that the resistive decay of the field leads to strong localized heating that in turn generates strong magnetosonic waves. Thus, the smaller p_0 and/or the larger A, the harder the test. We chose $p_0 = 0.1$ and $A = 0.3$ fairly close to the "standard" values quoted on the ATHENA web site[6], $p_0 = 0.05$ and $A = 0.1$. Here, we use an adiabatic exponent of $\gamma = 5/3$ and employ the conservative formulation of the scheme.

[6] `http://www.astro.princeton.edu/~jstone/tests/field-loop/Field-loop.html`

The test turns out to be very hard for PROTEUS, because of its low numerical diffusivity. Figure 2 summarizes the test results in the form of the total magnetic energy against time. The energy evolution splits into two branches: one corresponding to the lower-resolution models at all resistivities, and the other representing the higher-resolution models at $\lambda_\Omega = 0$ and $\lambda_\Omega = 10^{-5}$. At $\lambda_\Omega = 10^{-4}$, the field decay has converged: both resolutions give the same curve. At $N = 256^2$ and $\lambda_\Omega = 0$, the code crashes around $t = 6$. All other models run up to $t = 10$ and further.

The result confirms the discussion by Tang & Xu (2000), namely that while the conservative gas-kinetic flux splitting method in the BGK-formalism performs well for high-β plasmas (with β defined as the ratio of thermal over magnetic pressure), it might not be the method of choice for low-β plasmas, i.e. magnetically dominated systems. Note, however, that this is mainly a consequence of the scheme's conservative formulation. We experimented with a non-conservative version (i.e. just evolving the internal energy instead of the total energy), which was stable for lower p_0 and higher A, albeit at the cost of a less accurate total energy evolution.

2.2.3. *Advection of a Field Loop*

A cylindrical current distribution (i.e. a field loop) is advected diagonally across the simulation domain. We follow the implementation presented by Gardiner & Stone (2005) and the ATHENA test suite[6], based on an earlier version by Tóth & Odstrčil (1996). Density and pressure are both initially uniform at $n_0 = 1$ and $p = 1$, and the fluid is described as an ideal gas with an adiabatic exponent of $\gamma = 5/3$. The square grid ranges from $-0.5 \le x \le 0.5$, and the loop is advected at an angle of 30 degrees with respect to the x-axis. Thus, two round trips in x correspond to one crossing in y. The amplitude of the field loop is set to values 10^{-3}, 10^{-2} and 10^{-1}, with an initial radius of $R_0 = 0.3$. Figure 3 shows the initial current distribution with the magnetic field vectors over-plotted (*left*), and the final current distribution after two time-units measured in horizontal crossing times. The overall shape is preserved, although some artifacts are visible at the upper rim of the loop. These

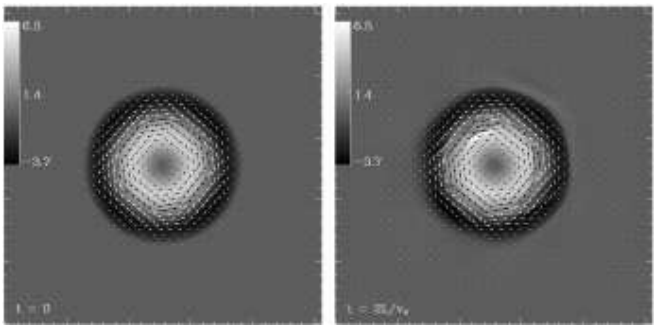

FIG. 3.— Current density for field loop advection test (see §2 2.2 2.2.3). *Left:* Initial condition. *Right:* After two horizontal crossings. The grid resolution is 256^2.

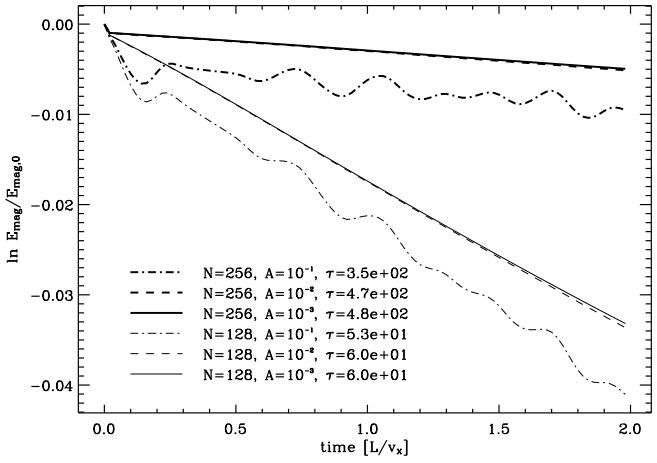

FIG. 4.— Normalized magnetic energy against time (in units of horizontal crossing time), for two resolutions and three field strengths. The highest amplitude leads to waves when perturbed by advection. At a resolution of 128^2, the magnetic energy has decayed by 3.3% after two crossing times. The fit decay times τ are indicated for each model.

results concerning the shape are qualitatively similar to those posted on the above mentioned website. Note that we show the current density, since the artifacts do not show up in the magnetic energy. This test uses $\lambda_\Omega \equiv 0$.

Figure 4 presents a quantitative diagnostic of the behavior of the code as it tracks the magnetic energy decay against the simulation time, in units of horizontal crossing times. The initial energy is normalized to one. Line styles denote different amplitudes of the field strength. The solid lines correspond to the case given by Gardiner & Stone (2005), the dashed and dash-dotted lines denote cases with larger amplitudes. At an amplitude of $A = 10^{-3}$ and a resolution of 128^2, the magnetic energy decays by 3.3% over two horizontal crossing times. The ATHENA website[6] quotes a decay of 3.5% with a $256x148$ grid, using a Roe solver and 3rd order reconstruction.

In summary, these numerical test cases demonstrate that PROTEUS models dissipative MHD effects accurately, due to a low intrinsic numerical diffusivity that compares well with that of higher-order Godunov methods. Furthermore, it can advect geometrically complex magnetic field patterns properly, and is well suited in its energy conserving form to model MHD flows with $\beta > 1$.

2.3. *Initial Conditions*

To remain as close as possible to Vishniac (1994), we will use the isothermal version of PROTEUS in the following. The initial conditions are similar to those discussed in Heitsch et al. (2005, 2006). Two uniform, identical flows in the x-y computational plane initially collide head-on at a sinusoidal interface with given wave number k_y and amplitude η. The field is either aligned or perpendicular to the inflow, but in both cases in the x-y plane. For the standard runs, we used a rectangular grid with an extent of 88 pc in x and 44 pc in y. Field strength as well as viscosity and resistivity are varied. The grid resolution varies between $N_x \times N_y = 256 \times 128$ and 2048×1024 by factors of 2 in linear resolution. The isothermal sound speed is $c_S = 5.3$ km s^{-1}, the Mach number of the instreaming gas is $\mathcal{M} = 4$, and the inflow density is set to $n_0 = 1$ cm^{-3}. Thus, in the code unit system, the Alfvén speed in the inflow region is given by $c_A = B$, the magnetic field strength.

3. RESULTS

We give a rough estimate for the field strength required to prevent the excitation of the NTSI in §3 3.1. The morphology of the instability naturally depends strongly on the field orientation. We present some examples in §3 3.2. Because of the strong shear flows, the explicit control of dissipation is crucial in reaching numerical convergence. This can be further quantified by monitoring the growth rates (§3 3.3). Finally, we show that the geometry of the flow and magnetic field strongly influence the field-density relation (§3 3.4).

3.1. *Estimate of Threshold Field Strength*

A very rough estimate of the threshold field strength preventing the excitation of the NTSI can be derived by simple pressure considerations. Figure 5 gives a sketch of the simplified situation. Only one half of the slab in the vertical direction is shown. The slab is displaced by η in the horizontal direction around the (dotted) center line. The angle between the slab and the symmetry line measured at point 0 is given by α, with $\tan\alpha \approx 2\eta k/\pi$. Gas is streaming in horizontally from the left and the right with velocity $\mathbf{u}$, and the magnetic field $\mathbf{B}$ is aligned with the inflow, pointing to the right. Incoming flow with positive velocities exerts a pressure at point 0, which can be split into a normal component $\overline{0D}$ and a tangential component $\overline{0F} = \overline{0E}\,\sin\alpha$. The tangential component corresponds to the ram pressure exerted by material deflected by the slab and sliding along $\overline{0F}$. To a zeroth order approximation, the component of this ram pressure perpendicular to $\mathbf{B}$ is available for bending the field lines, thus

$$\rho\, u^2\, \sin\alpha\, \cos\alpha \approx \mathbf{B}^2/2. \qquad (3)$$

The maximum is reached for $\alpha = \pi/4$, in which case $\rho u^2 \approx \mathbf{B}^2$. For an inflow velocity of $|u| = 4c_s$, we thus require a field strength corresponding to an Alfvén speed of $c_A \approx 4c_s$ to suppress the NTSI.

3.2. *Morphology*

We begin with our standard runs, in order to compare to Vishniac's analysis. These are the "laminar"

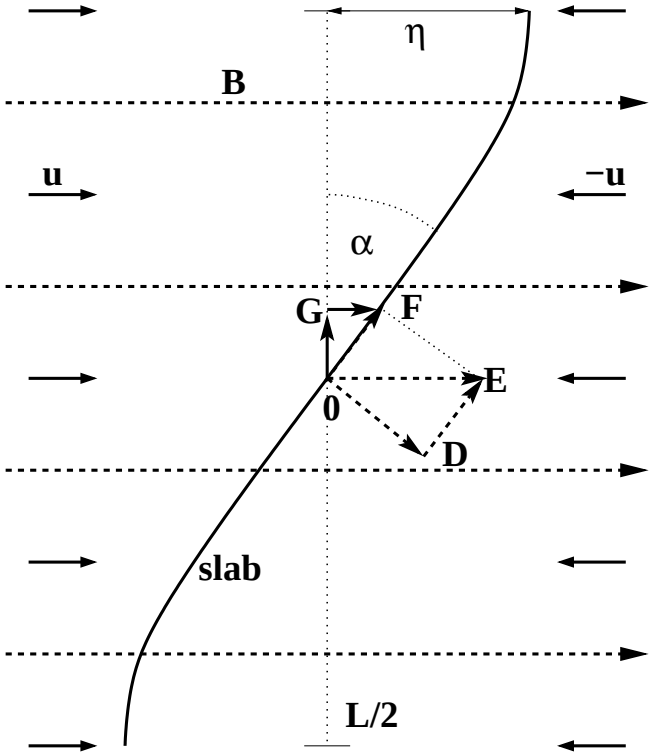

FIG. 5.— Sketch of force geometry for estimating the threshold field strength. A thick solid line marks the interface of the colliding flows (the "slab"). The magnetic field is represented by horizontal long short-dashed arrows, and inflow velocities by short solid ones. Other (force) vectors are defined in the text.

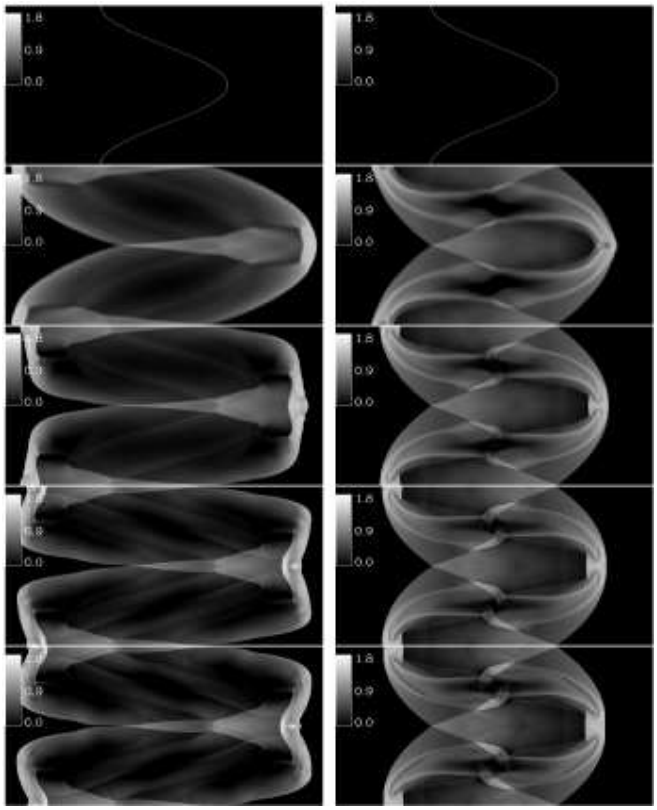

FIG. 6.— *Left column:* Logarithmic density maps of hydrodynamical models at $t = 3.8$ Myr corresponding to the end of simulation, resolution increasing from top to bottom ($N_x = 256$ to 2048 by factors of 2). The two highest resolutions have converged even in detail. *Right column:* Same as left, but for the magnetic models, where the field is aligned with inflow and $c_A/c_s = 1.0$. Again, the two highest resolutions have converged.

cases (§3 3.2 3.2.1), i.e. cases that do not develop turbulent substructure. The turbulent case and the relevance of fixed physical dissipation scales are discussed in §3 3.2 3.2.2.

3.2.1. *Laminar Case*

The left column of Figure 6 displays a model sequence in resolution for the hydro runs, corresponding to Vishniac's analysis. The top panel shows the initial condition (strictly, just after $t = 0$), The increasing overall amplitude of the slab signifies that the NTSI is clearly at work. Most of the gas is collected at the focal points, and by the end of the simulations, the system is close to saturation. The lowest resolution run differs from all others in that it is the only one for which numerical convergence has not been achieved. The two highest resolution runs ($N_x = 1024, 2048$, lower two panels), on the other hand have converged even in detail. Note that the viscosity and resistivity provide fixed physical dissipative scales, independent of the resolution. Thus, the model at $N_x = 256$ is not resolved with respect to these dissipative scales, while the high-resolution models are.

This is also true for the magnetic runs (right column of Figure 6) where the field has slowed down the growth of the NTSI. The resulting slab is also more structured than in the pure hydro case. High-density regions, especially thin filaments, coincide with regions of field reversals (loss of magnetic pressure support). To see this, one can compare the gas density to the magnetic energy (Figure 7) maps. The center column corresponds to the right column of Figure 6. Not only do the field reversals lead to dense structures, but magnetic waves arise. The left column of Figure 7 shows the same resolution sequence at half the field strength, i.e. $c_A/c_s = 0.5$, while the right column stands for $c_A/c_s = 2.0$. Higher field strengths not only reduce the growth rate of the NTSI, but also suppress the internal turbulent structure visible for $c_A/c_s = 0.5$. Numerical convergence is more easily achieved with higher field strength, which is another indicator that turbulence plays a minor role, i.e. we remain safely entrenched within the laminar regime. This is slightly different in the weak-field case where the two highest resolution runs have only mildly converged. Here, the field starts to get too weak to prevent the excitation of KHI modes.

A variation on the theme is shown in Figures 8 and 9 where the field is oriented vertically this time around. In a 1D geometry, the magnetic pressure would prevent the gas from efficiently accumulating to form high-density regions (i.e. clouds, see Bergin et al. 2004). The system would behave as if the gas had an adiabatic exponent of 2. This is the situation traced out by the models shown in the right column of Figures 8 and 9: because of the stiffened equation of state, high (flux-)density regions expand faster. However, high density is found at the focal points, hence the initial perturbation of the slab is smoothed out, and the slab ends up with plane-parallel shock fronts (due to the fields, there are some waves inside the slab,

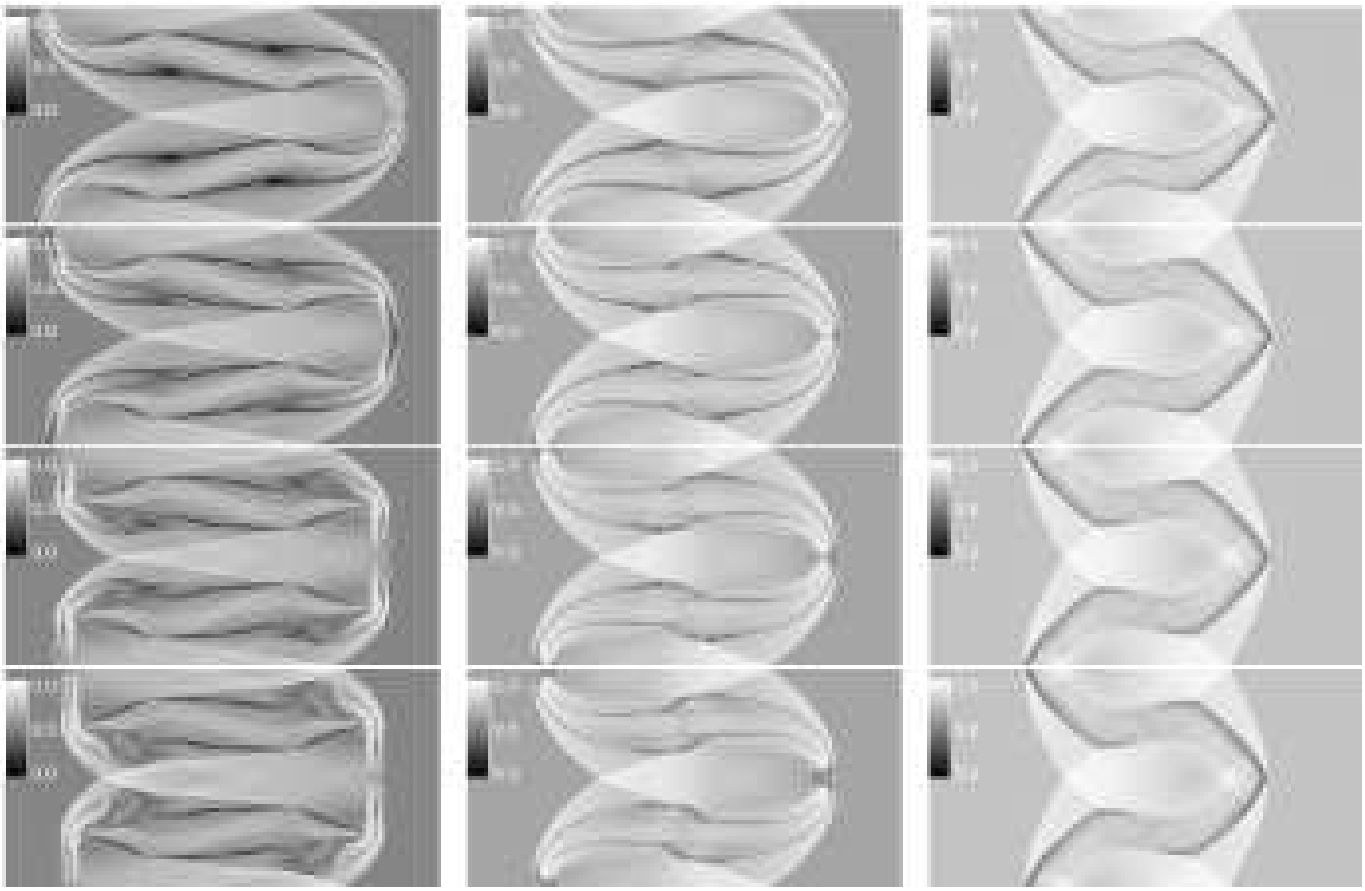

FIG. 7.— Logarithm of magnetic energy at $t = 3.8$ Myr. *Left:* Four resolutions increasing from top to bottom ($N_x = 256$ to 2048 by factors of 2) at $c_A/c_s = 0.5$. *Center:* For $c_A/c_s = 1.0$. *Right:* For $c_A/c_s = 2.0$.

though). Reducing the field strength (left column) by a factor of 2 however changes the situation drastically. Although the NTSI is only weak, high-density filaments start to form in the thick slab, again at the locations of field reversals. Thus, a transverse field is much less of an inhibiting factor for substructure or high-density region generation than what would be expected from a 1D-argument. For $c_A/c_s = 1.0$, the fast magnetosonic modes have already reached the boundaries, causing the geometric patterns visible in the density plot.

3.2.2. *Turbulent Case*

In the previous section, we discussed models with a fixed physical dissipative scale. The purpose of this section is to demonstrate that without a fixed dissipation scale, numerical convergence cannot be reached. In other words, for large Reynolds numbers, the system can evolve qualitatively differently.

Figure 10 shows a sequence in resolution of models with zero physical resistivity and viscosity, i.e. models for which the numerical dissipation at resolution scale will set the Reynolds number. Thus, higher resolution will lead to larger Reynolds numbers. For resolution reasons we chose the wave number of the interface perturbation to be $k = 1$ in §3 3.2 3.2.1. Since the condition for fast growth of the instability is given by $k\eta \approx 1$, this required a larger initial amplitude perturbation and an elongated box. Here, we are interested in the (later) turbulent evolution of the slab, thus we start with $k = 4$, which allows us to reduce the initial amplitude of the perturbation by the same factor 4 and therefore considerably extends the spatial range in which the slab can develop.

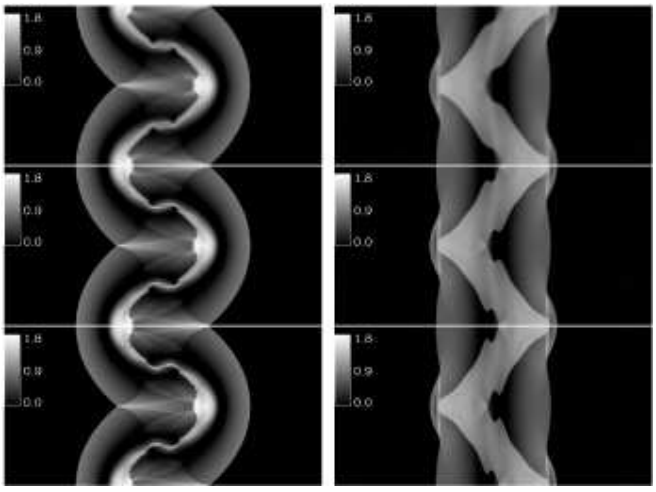

FIG. 8.— Logarithmic density maps for models with the field oriented transversally, i.e. perpendicular to the inflow, at $t = 3.8$ Myr. *Left:* Three resolutions increasing from top to bottom ($N_x = 256$ to 1024 by factors of 2) at $c_A/c_s = 0.5$. *Right:* For $c_A/c_s = 1.0$. The geometric pattern at the boundaries is an artifact caused by magnetosonic modes reaching the inflow boundaries.

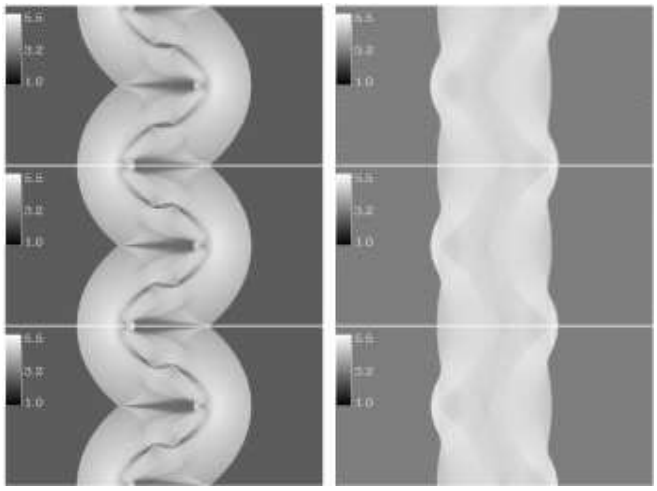

FIG. 9.— Logarithmic magnetic energy maps of models with the field oriented transversally, i.e. perpendicular to the inflow, at $t = 3.8$ Myr. *Left:* Three resolutions increasing from top to bottom ($N_x = 256$ to 1024 by factors of 2) at $c_A/c_s = 0.5$. *Right:* For $c_A/c_s = 1.0$.

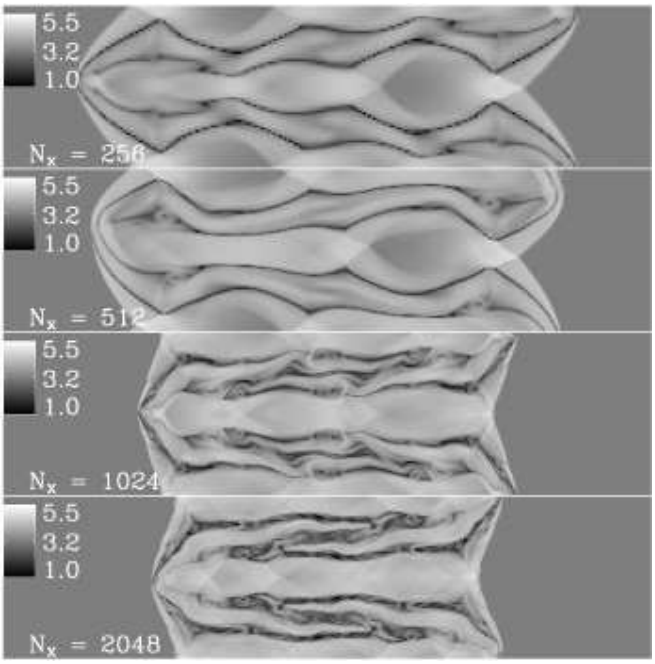

FIG. 10.— Logarithmic magnetic energy maps for models with viscosity $\nu \equiv 0$ and resistivity $\lambda_\Omega = 0$, i.e. the dissipation scale is given by the grid resolution. Resolution increases from top to bottom (256^2 to 2048^2 by factors of 2). Since the period in y is repeated four times, we show only one quarter of the domain. $t = 3.8$ Myr.

At our lowest resolution ($N_x = 256$), we essentially get a laminar behavior: the pairwise field reversal regions are stretched along the width of the slab but persist to the end of the simulation (top). At $N_x = 1024$, the main magnetic null regions are accompanied by secondary regions as a result of additional shear flows. The slab is thinner. Increasing the resolution further introduces more and more substructure in the slab, especially at the "heads" of the slab's perturbations: here, field reversals seem to accumulate, leading to additional field dissipation. Thus, with higher Reynolds numbers, the slab gets more turbulent, and reconnection proceeds not only in the two main magnetic null regions, but all throughout the slab in small regions. Consequently, turbulent field structures inside the slab are dissipated faster, leading to a deficit in magnetic pressure inside the slab, and thus to a thinner slab.

While this effect is certainly interesting to note, the situation might be less extreme in a truly three-dimensional system: a third field component without magnetic null could give rise to sufficient magnetic pressure to prevent reconnection (see also Heitsch & Zweibel 2003). In this case, small-scale fields entangled by the turbulence in the slab could actually lead to additional pressure.

The pressure profiles (Fig. 11) actually tell us a slightly more complicated story than that of simple magnetic energy dissipation. Pressures were averaged transversally (i.e. along the y-axis) and plotted against x, the inflow direction. The magnetic pressure profile stays pretty much at a constant level, independent of resolution and time. What changes is the kinetic pressure, which drops below its inflow value (all panels but bottom). This effect gets stronger with increasing resolution. Thus, the magnetic field only acts as a dissipation channel for the kinetic energy. One could even interpret the kinetic pressure drop and simultaneous magnetic and internal (red lines) pressure rise as an attempt of the system to achieve equipartition (Fig. 12).

This is not to say that the various pressure components are in equilibrium, as the left panel of Figure 13 easily demonstrates. This panel shows the correlation coefficient $\mathcal{C}$ for the three pairs of pressures, P_{mag}, P_{int}, and P_{kin}, for the case without (left) and with (right) a physical dissipation scale. Balance between the pressure components would show up as an anti-correlation, whereas a correlation can be interpreted as pressures being in phase (and thus driving waves). Decorrelated pressures indicate a mixture. Kinetic and magnetic pressure decorrelate at higher resolution, pointing to strong reconnection events. Internal and magnetic pressure are only slightly correlated (see below), while kinetic and internal pressure anti-correlate at late times, because high-density regions show more inertia. The models with a fixed physical dissipation scale do not show strong resolution effects. Note, however, that the "dissipation-less" models are farther in the dynamical evolution than the "controlled" models, because of the different initial conditions ($k_y = 4$ against $k_y = 1$).

These results demonstrate that only a fixed dissipative scale can guarantee full convergence of the models with resolution. Relying on numerical diffusion leads to flows with increasing Reynolds numbers as the resolution increases and results that depend qualitatively and quantitatively on resolution.

3.3. *Growth Rates*

Figure 14 summarizes the growth of the slab's amplitude with time. The hydrodynamical growth rates are consistent with the analytical predictions (eq. [1], solid straight black line). Saturation sets in when the focal points are shut off from the inflow (see also left column of Fig. 6). The two highest resolution runs have converged also in terms of growth rates (we established

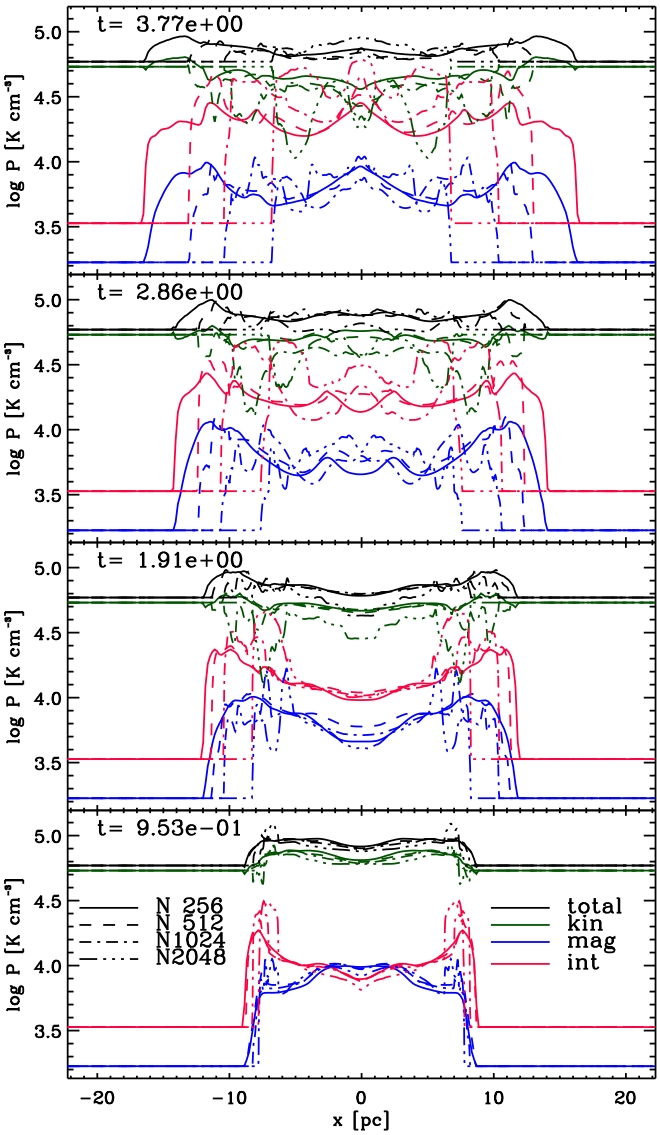

FIG. 11.— Transversally averaged pressure profiles for four times (in Myr), plotted in ascending time order from bottom to top, against x-axis coordinate. Shown are pressure profiles for magnetic models with $\nu \equiv 0$ and $\lambda_\Omega \equiv 0$ (see text). Gas is streaming in from the left and from the right. See bottom panel for color code and line styles. Shown are the total, the kinetic, the magnetic and the internal pressures.

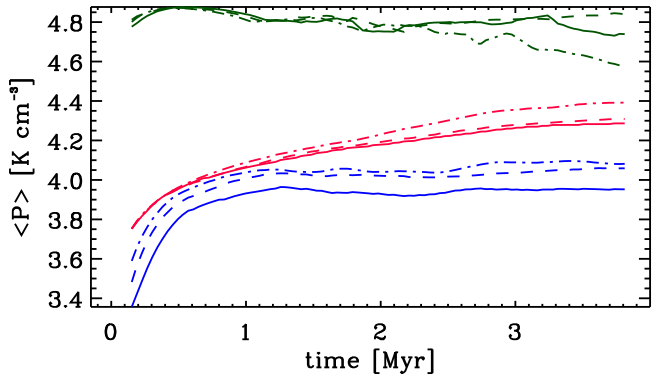

FIG. 12.— Average pressure in slab against time. Color coding and line style are the same as in Figure 11.

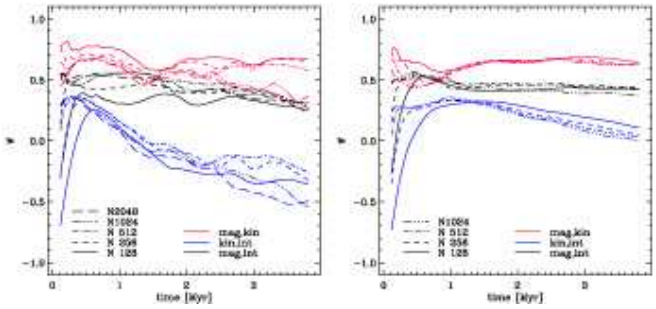

FIG. 13.— Correlation of pressures within slab against time. Line colors denote correlations, e.g. red stands for $\mathcal{C}(P_{mag}, P_{kin})$. Line styles denote resolution. *Left:* Models without fixed physical dissipation scales. *Right:* Viscous and resistive scales have been set.

detailed convergence in §3 3.2 3.2.1). Lower resolutions lead to slightly smaller amplitudes initially. The lowest resolution model is already resolved high enough to reproduce the laminar result, but the specified physical viscosity is too small to guarantee convergence with regards to turbulent substructure in the slab. Thus, when increasing to the next higher resolution, the unresolved turbulence leads to less converged growth rates. Note that the growth rate as given in equation (1) does not include the effect of turbulence generation within the slab, although the possible effects of turbulence are discussed by Vishniac (1994).

The dotted line in Figure 14 and all subsequent figures of the same type denotes the growth of the amplitude of an unperturbed shock-bounded slab of width $\Delta(t)$,

$$\Delta(t) = 2\, c_s\, t \left(\mathcal{M}/2 + (1 + (\mathcal{M}/2)^2)^{1/2} \right)^{-1} . \quad (4)$$

Thus, all models except for those with field strength $c_A/c_s = 2$ show a faster growth of the slab amplitude than just the shock-bounded expansion. Obviously, equation 3 only gives a rough estimate of the field strength required, and in fact underestimates the effect of the field. Our crude approximation treats the slab as a solid wall, allowing to split the pressure exerted by the inflow on the wall along the normal and tangential directions without any losses. This is most likely unrealistic, i.e. the tangential component will generally be smaller, thus requiring a smaller field to balance it.

With increasing field strength, the ordering of the curves with respect to resolution is inverted: now, the lowest-resolution runs show the fastest growth. Nevertheless we get convergence for the two highest resolution simulations. This inversion is a consequence of the slight increase in the Reynolds number with respect to the runs at lower resolution. As discussed above, higher Reynolds numbers lead to more turbulence and more field reversals. Thus, the field is dissipated faster, leading to a pressure deficit in the slab.

A vertical field leads to a strongly reduced growth rate or suppresses the instability completely, depending on its strength (Figure 15). The NTSI arises, however, for weaker field strengths, and the bending mode in the slab persists, thus allowing material to be funneled towards the focal points. In the presence of self-gravity or a strong thermal instability (e.g. that provided by atomic line cooling), these density enhancements could then frag-

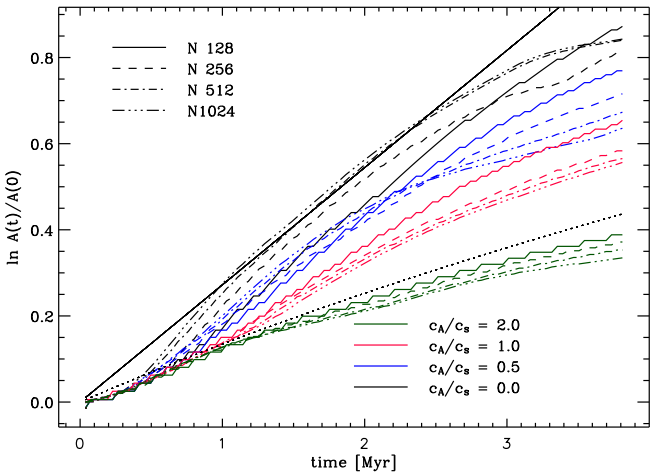

FIG. 14.— Slab amplitude against time for four models at zero field strength $c_A/c_s = 0$ to highest field strength $c_A/c_s = 2$. Line styles stand for resolution. The straight solid black line denotes the analytical solution (eq.[1], Vishniac 1994). The dotted line denotes the expansion of a shock-bounded unperturbed slab (eq. [4]).

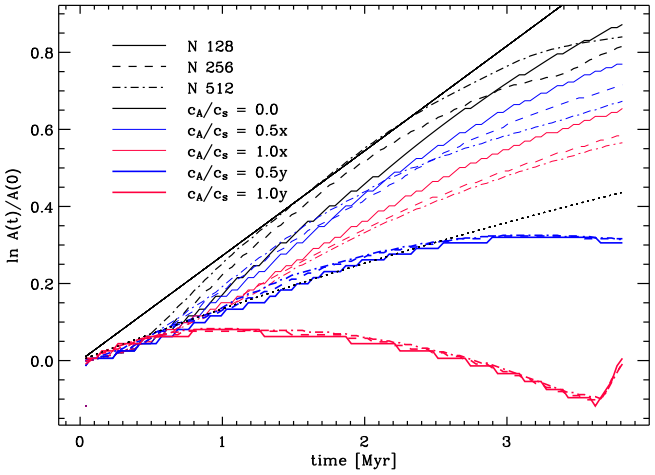

FIG. 15.— Slab amplitude against time for models with transverse fields. Thin lines denote the corresponding models with fields oriented along the inflow for comparison. Again, the straight solid black line denotes the analytical solution (eq. [1], Vishniac 1994). The dotted line denotes the expansion of a shock-bounded unperturbed slab (eq. [4]).

ment and generate further substructure, despite the initially unfavorable field orientation.

The amplitude growth corresponding to Figure 10 is shown in Figure 16. With higher resolution, saturation sets in earlier in the magnetic runs, and the amplitudes even decrease with time, mirroring the loss of pressure inside the slab due to (resistive) dissipation. Note that the slab amplitude now grows faster than that of an unperturbed shock-bounded slab (see dotted line in Fig. 16) only at times $t \lesssim 1$ Myr. As Figure 10 already had made us suspect, saturation sets in earlier for models with higher k.

3.4. *Field-Density Relation*

The field-density relation $B(n)$ is often used as an observational measure for the dynamical importance of magnetic fields in the interstellar medium. It describes the mass-loading of field lines, and is related to the

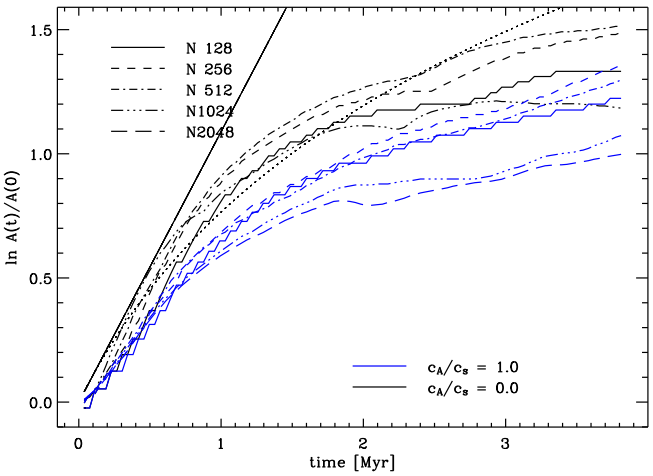

FIG. 16.— Slab amplitude against time for models with initial perturbation wave number $k = 4$ and without fixed resistive scale. Higher resolution leads to saturation of the growth rate at lower amplitudes. The straight solid black line denotes the analytical solution (eq. [1], Vishniac 1994). The dotted line denotes the expansion of a shock-bounded unperturbed slab (eq. [4]).

mass-to-flux ratio (e.g. Mouschovias & Spitzer 1976; Shu et al. 1987) quantifying the importance of magnetic fields in a gravitationally dominated cloud. Microscopically, the mass loading of field lines can be changed in two ways: by Ohmic diffusion and by ion-neutral (or ambipolar) drift. However, the two parameters controlling the degree to which the interstellar magnetic field is frozen to the gas are huge. The magnetic Reynolds number Re_M is the ratio of the Ohmic diffusion time to the dynamical time, and is typically of order $10^{15} - 10^{21}$. The second parameter, the ambipolar Reynolds number Re_{AD}, is the ratio of the ion-neutral drift time to the dynamical time. This number is typically many orders of magnitude less than the first one, and can approach unity in dense molecular gas. These numbers suggest that the magnetic field should be nearly perfectly frozen to the plasma component of the gas, and generally well frozen to the neutrals, except in the densest, nearly absolutely neutral regions. Thus, the $B(n)$ relation is determined primarily by dynamical rather than by microscopic processes. Parameterizing the relation by $q \equiv d\ln B/d\ln n$, one finds $q = 1$ for compression perpendicular to $\mathbf{B}$, $q = 2/3$ for isotropic compression, $q = 1/2$ for self-gravitating, magnetically sub-critical clouds (Fiedler & Mouschovias 1993), and $q = 0$ for compression parallel to $\mathbf{B}$.

Observations of the $B(n)$ relation in molecular gas indeed show that the strongest fields are associated with the densest gas (e.g. Crutcher 1999). However, in the more diffuse ISM, the $B(n)$ relation is consistent with $q \approx 0$ over 3 orders of magnitude in n (Troland & Heiles 1986, Heiles & Troland 2005). Thus, processes beyond microscopic diffusion are required to decouple field and density. The possibility of accelerating the decoupling through turbulent transport has been explored by Zweibel (2002) and Heitsch et al. (2004) (see also Kim & Diamond 2002, Fatuzzo & Adams 2002, and Li & Nakamura 2004). Numerical evidence for a weak $B(n)$ relation includes Padoan & Nordlund (1999) and de Avillez & Breitschwerdt (2005).

Figure 17 shows scatter plots of $\log B$ against $\log n$

for four models, each measured at $t = 4$ Myr. The top row shows models with the field parallel to the inflow (denoted by c_{Ax} in the label), while the field is oriented transversally, or perpendicularly to the inflow in the bottom row (denoted by c_{Ay}). Idealized scalings are indicated by the dashed lines.

The most striking difference between the top and the bottom row is that for the configuration where the field is parallel to the inflow, field and density seem to correlate more strongly than for the configuration where the field is perpendicular to the inflow. This might seem surprising at first. After all, one would expect the field to be correlated least with density if the gas is compressed along the field lines (top row), and to be correlated most with density when the gas is compressed perpendicularly to the field lines (bottom row). However, looking back at Figures 7 and 9 on the one hand, and Figure 10 on the other, we realize that the models with fields parallel to the inflow generally develop turbulence, leading to field line stretching. Thus, in the (denser) slab, the field generally will be stronger. Why, then, is there close to no correlation observable in the bottom row of Figure 17? The answer is hidden in the way we set up the initial conditions. To avoid the generation of strong MHD waves, we kept the field uniform, despite the fact that the flow collision interface is strongly perturbed (see top row of Fig. 6 for the initial conditions). Thus, when gas is deflected at the flanks (point "0" in Figure 5), it is essentially free to move along the field lines, i.e. transversally, but is increasingly prevented from continuing its trip towards the slab, because the magnetic pressure is increasing (note that the bulk magnetic field strength is higher in the bottom row of Fig. 17). Thus, the density can take on any values in the slab, while the field value is given by the ram pressure. A weaker field (lower right panel vs lower left panel of Figure 17) reduces this effect, allowing some scatter in the field strength, and, indeed, checking Figure 9 for this case, the slab actually shows substructure and is allowed to bend. Note that there is a strict $d\ln B/d\ln n = 1$ scaling for the strong field model (lower left panel), which results from the initial compression of the field lines.

While it is hard to generalize the results of our two-dimensional models, they demonstrate that the $B(n)$ relation is strongly influenced by the geometry of the fields and the gas flows. Even compression perpendicular to the field lines can lead to a nearly complete decoupling of field and density – as long as the gas flow is given the chance to break the symmetry.

In a sense, we expect the "geometrical" mechanism decoupling the field from the density (lower row of Figure 17) to compete with the turbulent transport of the magnetic field: both act on dynamical (flow) timescales. For fields oriented perpendicularly to the inflow, our models do not develop any substantial turbulence (this might also be due to a too small Reynolds number). On the other hand, the models with field parallel to the inflow direction do generate some turbulence. For these models, B and n decorrelate only at higher density values, corresponding to small scales, while the lower density regions show a reasonably well established correlation between B and n.

4. SUMMARY

The Non-linear Thin Shell Instability (NTSI, Vishniac 1994) is expected to occur in expanding shells, shocks or colliding gas streams. Previous studies have addressed the evolution of the NTSI under hydrodynamical conditions, including gravity and cooling. We have presented a numerical study of the NTSI including magnetic fields. We have established that our numerical method is well suited to tackle the problem. We have found that the effects of magnetic fields on the NTSI can be summarized as follows:

(1) Fields principally tend to weaken or even suppress the NTSI. We further distinguish between two cases: (i) fields aligned with the inflow resist the transverse momentum transport – which is the main driving agent of the NTSI – via the magnetic tension force; (ii) fields perpendicular to the inflow lead to a stiffer equation of state. If $c_A \approx u$, the NTSI is suppressed. However, even for transverse fields, substructures can form within the slab, which can serve as fragmentation seeds in the presence of thermal instabilities or self-gravity.

(2) A fixed physical scale both for viscous and resistive dissipation is necessary to reach numerical convergence. When relying on numerical dissipation at the resolution scale, the Reynolds number will increase with resolution, leading to a more turbulent environment and thus to results which qualitatively and quantitatively depend on resolution (Figs 7, 10 and 16).

(3) At larger Reynolds numbers, turbulent reconnection plays a role in the turbulent dense slab generated by the NTSI. Magnetic energy is therefore dissipated at higher rates, leading to a pressure deficit in the dense slab. The magnetic field acts as a dissipation channel (Figs 11 and 12).

(4) Although the energies (or average pressures) seem to show a tendency of the system to evolve towards equipartition, pressures do not balance locally within the slab (Figs. 12 and 13). Correlated pressures lead to waves, i.e. the slab's inner structure is highly dynamical.

(5) The relation between field and density is, at best, weak in all models (Fig. 17). Models with fields parallel to the inflow exhibit a stronger $B(n)$ correlation than models with fields oriented perpendicularly to the inflow. The main reason for this is the generation of turbulence, which leads to field line stretching and thus field amplification within the denser slab. Fields oriented perpendicularly to the inflow allow instreaming material to move laterally, permitting the field and density to decorrelate.

Our isothermal models only allow a limited exploration of the effect of fields on colliding flows in a thermally or gravitationally unstable medium. Clearly, substructure can form in the slab under most conditions, providing potential seeds for thermal or gravitational instabilities. Thus, to establish the role of magnetic fields for molecular cloud formation in the colliding flow scenario, the thermal and gravitational effects have to be addressed.

We thank E. Zweibel for a critical reading of the manuscript and for enlightening discussions, and E. Vishniac for comments on magnetic field effects in the NTSI. Computations were performed at the NCSA (AST040026) and on the local resources at U of M, perfectly administered and maintained by J. Hallum. This work was supported by the University of Michigan and

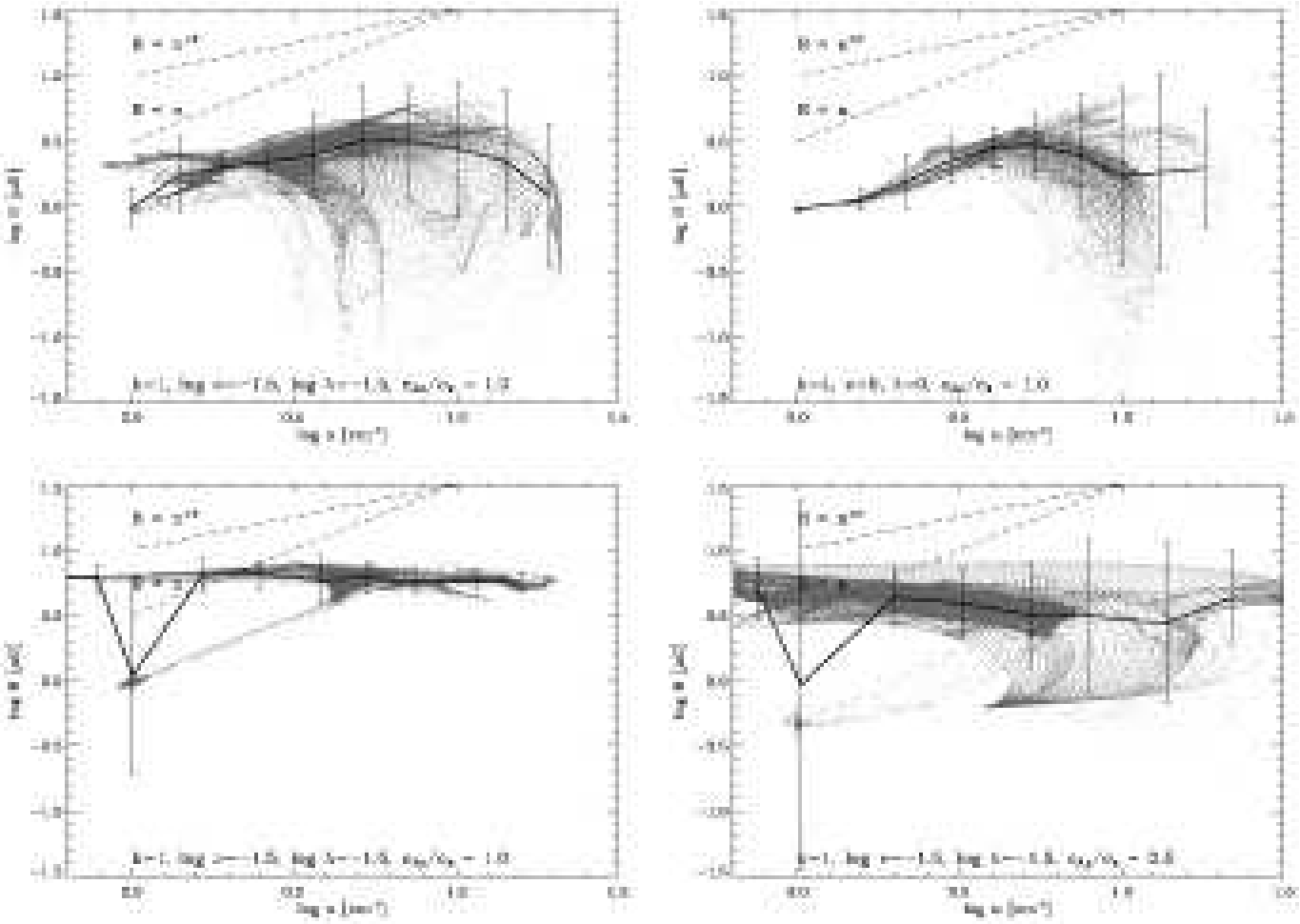

FIG. 17.— Scatter plots of magnetic field strength $\log B$ against density $\log n$ for models with parameters indicated in panels. Dashed lines denote idealized $B(n)$-scalings.

has made use of the NASA Astrophysics Data System.

REFERENCES

Balsara, D. S. 1998, ApJS, 116, 133
Bergin, E. A., Hartmann, L. W., Raymond, J. C., & Ballesteros-Paredes, J. 2004, ApJ, 612, 921
Bhatnagar, P. L., Gross, E. P., & Krook, M. 1954, Physical Review, 94, 511
Blondin, J. M. & Marks, B. S. 1996, New Astronomy, 1, 235
Boldyrev, S., Nordlund, Å., & Padoan, P. 2002, Physical Review Letters, 89, 031102
Cho, J. & Lazarian, A. 2003, MNRAS, 345, 325
Crutcher, R. M. 1999, ApJ, 520, 706
de Avillez, M. A. & Breitschwerdt, D. 2005, A&A, 436, 585
Elmegreen, B. G. & Scalo, J. 2004, ARA&A, 42, 211
Falgarone, E., Lis, D. C., Phillips, T. G., Pouquet, A., Porter, D. H., & Woodward, P. R. 1994, ApJ, 436, 728
Fatuzzo, M. & Adams, F. C. 2002, ApJ, 570, 210
Fiedler, R. A. & Mouschovias, T. C. 1993, ApJ, 415, 680
Gardiner, T. A. & Stone, J. M. 2005, Journal of Computational Physics, 205, 509
Goldreich, P. & Sridhar, S. 1995, ApJ, 438, 763
Hartmann, L., Ballesteros-Paredes, J., & Bergin, E. A. 2001, ApJ, 562, 852
Hawley, J. F. & Stone, J. M. 1995, Comp. Phys. Comm., 89, 127
Heiles, C. & Troland, T. H. 2005, ApJ, 624, 773
Heitsch, F., Burkert, A., Hartmann, L. W., Slyz, A. D., & Devriendt, J. E. G. 2005, ApJ, 633, L113
Heitsch, F., Slyz, A. D., Devriendt, J. E. G., Hartmann, L. W., & Burkert, A. 2006, ApJ, 648, 1052
Heitsch, F. & Zweibel, E. G. 2003, ApJ, 590, 291
Heitsch, F., Zweibel, E. G., Slyz, A. D., & Devriendt, J. E. G. 2004, ApJ, 603, 165
Hueckstaedt, R. M. 2003, New Astronomy, 8, 295
Kim, E.-j. & Diamond, P. H. 2002, ApJ, 578, L113
Klein, R. I. & Woods, D. T. 1998, ApJ, 497, 777
Li, Z.-Y. & Nakamura, F. 2004, ApJ, 609, L83
Mouschovias, T. C. & Spitzer, Jr., L. 1976, ApJ, 210, 326
Padoan, P. & Nordlund, Å. 1999, ApJ, 526, 279
Palotti, M. L., Heitsch, F., Zweibel, E. G., & Huang, Y.-M. 2006, ApJ, submitted
Passot, T., Vázquez-Semadeni, E., & Pouquet, A. 1995, ApJ, 455, 536
Prendergast, K. H. & Xu, K. 1993, Journal of Computational Physics, 109, 53
Shu, C.-W. & Osher, S. 1988, J. Chem. Phys., 77, 439
Shu, F. H., Adams, F. C., & Lizano, S. 1987, ARA&A, 25, 23
Slyz, A., Devriendt, J. E. G., Bryan, G. L., Heitsch, F., & Silk, J. 2006, MNRAS, submitted
Slyz, A. & Prendergast, K. H. 1999, A&AS, 139, 199
Tang, H.-Z. & Xu, K. 2000, J. Chem. Phys., 165, 69
Tóth, G. & Odstrčil, D. 1996, J. Chem. Phys., 182, 82
Troland, T. H. & Heiles, C. 1986, ApJ, 301, 339
Vázquez-Semadeni, E., Passot, T., & Pouquet, A. 1995, ApJ, 441, 702
Vázquez-Semadeni, E., Ryu, D., Passot, T., González, R. F., & Gazol, A. 2006, ApJ, 643, 245

Vishniac, E. T. 1994, ApJ, 428, 186
Xu, K. 1999, J. Chem. Phys., 153, 334
Zachary, A. L., Malagoli, A., & Collella, P. 1994, J. Sci. Stat. Comput., 15, 263
Zweibel, E. G. 2002, ApJ, 567, 962